Exp. Fluids manuscript No.
(will be inserted by the editor)

Full-field pressure from snapshot and time-resolved volumetric PIV

A. Laskari · R. de Kat · B. Ganapathisubramani

Received: date / Accepted: date

Abstract This paper deals with pressure estimation from snapshot and time-resolved three component (3C) volumetric PIV data using Taylor's hypothesis, an Eulerian and a pseudo-Lagrangian approach. The Taylor's hypothesis approach has been shown to provide accurate results for pressure in the case of 3C planar PIV data with an appropriate choice of convection velocity (de Kat and Ganapathisubramani, 2013) and here we extend its use on 3C volumetric velocity snapshots. Application of the techniques to synthetic data shows that the Taylor's hypothesis approach performs best using the streamwise mean as the convection velocity and is affected the least by noise, while the Eulerian approach suffers the most. In terms of resolution, the pseudo-Lagrangian approach is the most sensitive. Its accuracy can be improved by increasing the frame time-separation when computing the material derivative, at the expense of volume loss from fluid parcels leaving the FOV. Comparison of the techniques on turbulent boundary layer data with DNS supports these observations and shows that the Taylor's hypothesis approach is the only way we can get pressure when time information is not present.

Keywords Pressure from PIV, Taylor's hypothesis, Eulerian, Lagrangian, acceleration

1 Introduction

Flow pressure information is essential in various engineering applications, yet there are still difficulties involved when measuring it directly. In recent years, techniques for indirect pressure extraction have been developing. They involve using PIV velocity data and exploiting the link between pressure and velocity, stemming from the Navier–Stokes (NS) equations, to derive pressure. Following this line of work, Gurka et al (1999) used planar PIV velocity data to compute pressure distributions of a water flow in a pipe and of an impinging air jet and compared the results with reported data from previous studies. Fujisawa et al (2005) also used PIV velocity data to numerically solve the pressure Poisson equation to acquire pressure and fluid forces on a circular cylinder. Liu and Katz (2006) estimated material accelerations from PIV velocity data, which they subsequently integrated applying an omni-directional virtual boundary integration scheme. De Kat et al (2008) acquired planar pressure fields, starting from time-resolved PIV velocity data of a flow past a square-section cylinder and using a Poisson solver and they compared the results with surface pressure measurements. Later on, Charonko et al (2010) implemented different Eulerian methods for pressure determination, using both numerical and experimental velocity data, and assessed their dependence on grid resolution, sampling rate, measurement error, and off-axis recording.

Many of these studies used Eulerian methods to compute the material acceleration term. However, the acceleration can also be determined using a Lagrangian approach and the comparison of the two methods has also been the focus of several recent works. Using PIV on surface waves to predict flow accelerations and forces, Jakobsen et al (1997) compared Eulerian and Lagrangian approaches and the results indicated that the former approach matched closely the analytical calculations. The Lagrangian approach exhibited a small bias, which led to a systematic error in the estimation of flow acceleration and seemed to be limited due to poor tracking or deformation of fluid volume. This observation was supported by de Kat and van Oudheusden (2012), who found that a pseudo-Lagrangian approach (reconstruct-

A. Laskari · R. de Kat · B. Ganapathisubramani
Aerodynamics and Flight Mechanics Research Group, University of Southampton, Southampton SO17 1BJ, UK
E-mail: a.laskari@soton.ac.uk and r.de-kat@soton.ac.uk and g.bharath@soton.ac.uk

ing fluid parcel paths from velocity fields, in contrast with particle path tracking of LA-techniques) limited in time by the turnover time of the structures, exhibited more severe restrictions than an Eulerian one, requiring thick measurement volumes to accurately reconstruct the fluid path. They also showed that the Eulerian approach suffered more from measurement noise and was limited in time by the advection of structures on the boundaries, but not as much as the pseudo-Lagrangian (de Kat and van Oudheusden, 2012). In contrast to these findings, results from pressure field evaluation of rod–airfoil flow from time-resolved PIV (Violato et al, 2010) suggested that a pseudo-Lagrangian approach managed a lower precision error with a larger timestep than an Eulerian one, which was again shown to suffer from measurement noise. In line with this, Ghaemi et al (2012), used time-resolved, Tomographic PIV (Tomo-PIV) on a turbulent boundary layer to estimate pressure and showed that a pseudo-Lagrangian formulation performed much better than an Eulerian one, when compared with microphone surface pressure measurements.

In view of these developments and contrasting results, an alternative method was proposed by de Kat and Ganapathisubramani (2013). It was based on an Eulerian approach but avoided its aforementioned temporal limitations by using Taylor's hypothesis for the estimation of the flow acceleration. The technique was successfully implemented on both synthetic and experimental 3C planar velocity data and results indicated that pressure could be accurately estimated with an appropriate choice of convection velocity (de Kat and Ganapathisubramani, 2013). In this work, we extend the use of Taylor's hypothesis to estimate pressure on three-component volumetric velocity snapshots and compare the results with those of an Eulerian and a pseudo-Lagrangian approach. The three different methods are described and a linear uncertainty propagation analysis is performed to estimate the uncertainty on the resulting pressure fields. A numerical assessment is then carried out using the channel flow database from John's Hopkins University (Li et al, 2008; Perlman et al, 2007; Graham et al, 2013). The dependence of all methods on grid resolution and noise levels is tested, as well as the influence of time separation between frames on the Eulerian and pseudo-Lagrangian approaches and of different convection velocities on Taylor's hypothesis. Finally, the methods are implemented on time-resolved Tomo-PIV data from a turbulent boundary layer and the resulting pressure fields and statistics are compared with each other and with DNS results.

2 Method description

Throughout this paper, we use the coordinate system x, y, and z to denote the streamwise, wall-normal and spanwise directions respectively and u, v, w to denote the corresponding velocity components. The incompressible NS equations can be rewritten, solving for the pressure gradient, as follows:

$$\nabla p = -\rho \left\{ \frac{\partial \mathbf{u}}{\partial t} + (\mathbf{u}\cdot\nabla)\,\mathbf{u} - \nu\nabla^2\mathbf{u} \right\} \tag{1}$$

where $\mathbf{u}$ is the velocity vector field, p is the pressure field, ρ is the fluid's density and ν its kinematic viscosity. Taking the divergence of the pressure gradient, the result is a Poisson equation (2), which can be solved by spatial integration using a Poisson solver (see de Kat and Ganapathisubramani, 2013). The boundary conditions used are Neumann using eq. (1).

$$\begin{aligned} \nabla\cdot\nabla p &= \frac{\partial^2 p}{\partial x^2} + \frac{\partial^2 p}{\partial y^2} + \frac{\partial^2 p}{\partial z^2} \\ &= \frac{\partial}{\partial x}\left(\frac{\partial p}{\partial x}\right) + \frac{\partial}{\partial y}\left(\frac{\partial p}{\partial y}\right) + \frac{\partial}{\partial z}\left(\frac{\partial p}{\partial z}\right) \end{aligned} \tag{2}$$

The convective and viscous terms in eq. (1) can be readily computed, from full 3D velocity fields. If time information is also provided (time-resolved measurements), the acceleration can be computed using an Eulerian or a Lagrangian approach and the pressure gradients are fully defined. It is important to also note that, by taking the divergence of the pressure gradient and using the continuity equation, the viscous term drops out in the Poisson formulation.

2.1 Eulerian approach (EU)

Assuming that the temporal velocity gradient is approximately constant or linear in time within the time interval between the two snapshots, dt, and for all spatial locations (Jakobsen et al, 1997), the acceleration at time t (eq. 3), as well as the pressure gradient (eq. 4) can then be evaluated.

$$\frac{\partial \mathbf{u}}{\partial t} = \frac{1}{2dt}\left\{ \mathbf{u}|_{(\mathbf{x},t+dt)} - \mathbf{u}|_{(\mathbf{x},t-dt)} \right\} \tag{3}$$

$$\nabla p = -\rho \left\{ \frac{1}{2dt}\left\{ \mathbf{u}|_{(\mathbf{x},t+dt)} - \mathbf{u}|_{(\mathbf{x},t-dt)} \right\} + (\mathbf{u}\cdot\nabla)\,\mathbf{u} - \nu\nabla^2\mathbf{u} \right\} \tag{4}$$

For time-resolved data, another common approach to compute the material acceleration is by following particle trajectories (Lagrangian). A pseudo-Lagrangian approach is outlined in the next section.

2.2 Pseudo-Lagrangian approach (pLA)

Following de Kat and van Oudheusden (2012), we define a pseudo-Lagrangian description of the flow by reconstructing fluid-parcel trajectories using a pseudo-tracking approach. More specifically, using Taylor's expansion for a time interval, τ and following an iterative procedure, any fluid-parcel particle trajectory can be estimated for iteration k, as follows:

$$\mathbf{x}_p^k(t,\tau) = \mathbf{x} + \mathbf{u}(\mathbf{x},t)\tau + \frac{1}{2}\frac{D\mathbf{u}}{Dt}^k(\mathbf{x},t)\tau^2 \tag{5}$$

At the next iteration level, indicated with the subscript $k+1$, the material acceleration is then computed (eq. 6) and the pressure gradient (eq. 1) can be fully determined (eq. 7).

$$\frac{D\mathbf{u}}{Dt}^{k+1}(\mathbf{x},t) = \frac{\mathbf{u}(\mathbf{x}_p^k(t,\Delta t),t+\Delta t) - \mathbf{u}(\mathbf{x}_p^k(t,-\Delta t),t-\Delta t)}{2\Delta t} \tag{6}$$

$$\nabla p = -\rho\left\{\frac{D\mathbf{u}}{Dt}(\mathbf{x},t) - \nu\nabla^2\mathbf{u}\right\} \tag{7}$$

Even though here we focus only on a pseudo-Lagrangian approach, for completeness it should also be noted that recently, new techniques have been developed that allow for highly accurate, fully Lagrangian particle tracking information. Most notably, Schanz et al (2013, 2014) developed the 'Shake the Box' algorithm (STB) which, for a single timestep, reconstructs a particle track for previous timesteps, predicts the position of the particle in the next timestep and corrects this position by shaking the particles to fit in the measurement volume, using image matching (Schanz et al, 2014). The procedure is completed by finding new particles and their tracks, removing those that left the volume and repeating the image matching where necessary. It was shown that when converged, STB can accurately detect almost all particles residing in the measurement volume with fairly low position errors. In this way, velocity gradients and material acceleration information—that are very difficult to estimate accurately from PIV data—become available and provide a very promising input to the pressure estimation schemes discussed above.

Regardless of the reconstruction method used though, acquiring three-dimensional, time-resolved data is challenging and in cases where this is not possible, alternative methods have to be used, such as a Taylor's hypothesis approach which is described in the following section.

2.3 Taylor's hypothesis approach (TH)

Taylor's hypothesis states that, if the mean velocity is significantly larger than turbulent fluctuations, turbulent eddies are 'frozen' in time and are simply convected by the mean flow (Taylor, 1938). In the case of grid generated decaying turbulence, for which it was originally developed, the hypothesis was shown to perform well (Favre et al, 1955). In shear flows however, which are of interest here, the hypothesis breaks down (Lin, 1953) since the turbulent fluctuations are transported with convection velocities that differ from the mean (Fisher and Davies 1964; Zaman and Hussain 1981; Kim and Hussain 1993; Davoust and Jacquin 2011, among others). Structures of different sizes are expected to behave differently and even different parts of the same structure might move with different velocities as the structure evolves over time, making a complete definition of the convection velocity quite challenging (Krogstad et al, 1998). Previous studies have used spectral information to estimate it, showing that small scales are indeed travelling with the local mean following the original form of Taylor's hypothesis however this is not true for low frequencies corresponding in larger modes (del Álamo and Jiménez, 2009; Davoust and Jacquin, 2011). De Kat and Ganapathisubramani (2013) showed that using an in-plane filtered axial velocity in a turbulent jet as the convection velocity, yields more promising results for pressure, than using the mean. More recently, Geng et al (2015) tested the validity of using the mean as the convection velocity in the case of a turbulent channel and concluded that the assumption holds well in the logarithmic and outer layer but fails close to the wall. In the present study, different convection velocities will be tested, so a generalised form of Taylor's hypothesis, with a spatially changing convection velocity, $\mathbf{U_c} = (U_c, V_c, W_c)$ will be used:

$$\frac{D\mathbf{u}'}{Dt} = \frac{\partial\mathbf{u}'}{\partial t} + (\mathbf{U_c}\cdot\nabla)\,\mathbf{u}' = 0 \tag{8}$$

When only volumetric velocity snapshots are available (3D-volumetric PIV or DNS), the missing temporal information can then be extracted from eq. (8) as:

$$\frac{\partial\mathbf{u}'}{\partial t} = -(\mathbf{U_c}\cdot\nabla)\,\mathbf{u}' \tag{9}$$

To examine the implications of using this hypothesis on the governing equations, we start from the momentum equation, rewriting it so as to include the chosen convection velocity (see Geng et al, 2015) and using Reynold's decomposition:

$$\frac{\partial\mathbf{u}}{\partial t} = -\left\{\frac{1}{\rho}\nabla p + (\mathbf{u}\cdot\nabla)\,\mathbf{u} - \nu\nabla^2\mathbf{u}\right\} \Rightarrow$$

$$\begin{aligned}\frac{\partial\mathbf{u}'}{\partial t} = &-(\mathbf{U_c}\cdot\nabla)\,\mathbf{u}' - \left\{\frac{1}{\rho}\nabla p + ([\mathbf{U}-\mathbf{U_c}]\cdot\nabla)\mathbf{u}'\right.\\ &\left.+ (\mathbf{u}'\cdot\nabla)\,\mathbf{u} + (\mathbf{U}\cdot\nabla)\,\mathbf{U} - \nu\nabla^2\mathbf{u}\right\}\end{aligned} \tag{10}$$

It is then clear that, Taylor's hypothesis is well satisfied, if the *sum* of the pressure, convective and viscous terms (enclosed in brackets) is negligible (Geng et al, 2015).

$$\frac{1}{\rho}\nabla p + ([\mathbf{U}-\mathbf{U_c}]\cdot\nabla)\mathbf{u}' + (\mathbf{u}'\cdot\nabla)\,\mathbf{u} + (\mathbf{U}\cdot\nabla)\,\mathbf{U} - \nu\nabla^2\mathbf{u} = 0 \quad \Rightarrow$$

$$\nabla p = -\rho\,\{([\mathbf{U}-\mathbf{U_c}]\cdot\nabla)\mathbf{u}' + (\mathbf{u}'\cdot\nabla)\mathbf{u} + (\mathbf{U}\cdot\nabla)\,\mathbf{U} - \nu\nabla^2\mathbf{u}\} \tag{11}$$

It is then the last equation, that fully determines the pressure gradient, which is subsequently integrated and solved (eq. 2). It should be noted here that, the term $(\mathbf{U}\cdot\nabla)\mathbf{U}$ is generally small for fully convective flows, however it was included here for completeness. In regions where the choice of convection velocity is not correct, the pressure gradient equation is no longer balanced and the resulting pressure fields start to deviate from the exact solution.

3 Uncertainty estimates

In this work, pressure is estimated from experimental—and therefore imperfect—velocity data. It is then important to evaluate how an initial uncertainty, ε_u, on the velocity field would propagate down to the derived quantity, namely here, pressure. Following a linear uncertainty propagation procedure, outlined by de Kat and van Oudheusden (2012) (for more details see JCGM 100:2008) each measured quantity, x, involved in the estimation of a derived quantity, r, is associated with its uncertainty, ε_x, and its sensitivity coefficient, $\theta_x = \partial r/\partial x$, which determines the influence of this uncertainty on the uncertainty of the derived quantity. The product of the uncertainty with the sensitivity coefficient gives the contribution of each measured quantity, x, towards the total uncertainty of the derived quantity. This total uncertainty, ε_r, is proportional to the square root of the sum of the square of the contributions from all the measured quantities involved in the derivation. More specifically, using eq. (4), the total uncertainty on the pressure field using EU can be written as:

$$\varepsilon_{P,EU} \propto \varepsilon_u \sqrt{\Big[\underbrace{\frac{1}{2}\Big(\frac{h}{\Delta t}\Big)^2}_{I} + \underbrace{\frac{|\mathbf{u}|^2}{2}}_{II} + \underbrace{h^2\frac{|\nabla u|^2+|\nabla v|^2+|\nabla w|^2}{3}}_{III}\Big]} \tag{12}$$

where $\varepsilon_{P,EU}$ is the total uncertainty on the estimated pressure field, Δt is the time separation of the velocity fields, $|\mathbf{u}|$ is the magnitude of the velocity vector, $|\nabla u|$, $|\nabla v|$, and $|\nabla w|$ are the magnitudes of the streamwise, wall-normal and spanwise velocity gradients respectively and $h = \Delta x = \Delta y = \Delta z$, is the grid resolution.

Considering a linear fluid-parcel trajectory and following eq. (5) and (6) once, the total uncertainty on the estimated pressure field for pLA is:

$$\varepsilon_{P,pLA} \propto \varepsilon_u \sqrt{\Big[\underbrace{\frac{1}{2}\Big(\frac{h}{\Delta t}\Big)^2}_{I} + \underbrace{h^2\frac{|\nabla u|^2+|\nabla v|^2+|\nabla w|^2}{6}}_{III}\Big]} \tag{13}$$

Finally, for TH, following eq. (11), the total uncertainty on the resulting pressure field can be estimated as follows:

$$\varepsilon_{P,TH} \propto \varepsilon_{U_c}\sqrt{\Big[\underbrace{h^2\frac{|\nabla u'|^2+|\nabla v'|^2+|\nabla w'|^2}{3}}_{III}\Big]} + \varepsilon_U A_U + \varepsilon_u\sqrt{\Big[\underbrace{\frac{1}{2}|\mathbf{U}-\mathbf{U_c}|^2+\frac{|\mathbf{u}'|^2}{2}}_{II} + \underbrace{h^2\frac{|\nabla u|^2+|\nabla v|^2+|\nabla w|^2}{3}}_{III}\Big]} \tag{14}$$

where $\varepsilon_{P,TH}$ is the total uncertainty on the estimated pressure field, ε_{U_c} is the uncertainty on the convection velocity estimation, ε_U is the uncertainty on the mean velocity, $|\mathbf{u}'|$ is the magnitude of the velocity fluctuation and $|\nabla u'|$,$|\nabla v'|$,$|\nabla w'|$ are the magnitudes of the gradient of the streamwise, wall-normal and spanwise velocity fluctuation components respectively. With A_U we denote the sensitivity coefficient of the uncertainty on the mean velocity, which is defined as follows:

$$A_U = \sqrt{\Big[\frac{1}{2}|\mathbf{U}-\mathbf{U_c}|^2+h^2\frac{|\nabla u|^2+|\nabla v|^2+|\nabla w|^2}{3}\Big]} + \sqrt{\Big[+\frac{|\mathbf{U}|^2}{2}+h^2\frac{|\nabla u'|^2+|\nabla v'|^2+|\nabla w'|^2}{3}\Big]} + \sqrt{\Big[h^2\frac{|\nabla U|^2+|\nabla V|^2+|\nabla W|^2}{3}\Big]} \tag{15}$$

For all methods, the letters *I*, *II*, and *III* are used to denote the uncertainties corresponding to the time, velocity and velocity gradient terms respectively, for reference in the sections that follow. For TH only the terms related to the uncertainty in the total velocity field, ε_u, and in the convection velocity, ε_{U_c} are highlighted, since for well converged mean fields, ε_U is expected to be small (as a statistical uncertainty) and its contribution inconsequential with respect to the other terms. It should also be noted here that, for all methods, the uncertainty from the viscous term is neglected because, as mentioned above, the viscous term present in the pressure gradient equation drops out in the Poisson formulation.

Using equations (12)–(14) on a single DNS velocity volume (see sect. 4)—to have a realistic estimate of the velocity and gradient terms—the total uncertainty on the pressure estimation for each method is computed, for increasing levels

of measurement uncertainty on the velocity field (fig. 1a). For TH (using the streamwise mean velocity as the convection velocity), different levels of the convection velocity uncertainty, ε_{U_c}, and mean velocity uncertainty, ε_U, are also presented (fig. 1b). As already mentioned, for zero measurement noise on the velocity field, both EU and pLA have zero uncertainty propagating on the estimated pressure. With increasing velocity uncertainty level, there is a linear increase in the resulting uncertainty in pressure for both methods, with EU having a much steeper increase due to the extra velocity term, II, in eq. 12. For TH, if both the uncertainty on the convection and mean velocity are zero, the propagation uncertainty on the pressure is zero as well (fig. 1a and lower limit, fig. 1b). However, a perfect estimate for the convection velocity is unlikely to be found, so a more realistic situation would include uncertainties on both the convection and the mean velocity (fig. 1b) with the latter being minimal, as already mentioned above. In the case of a moderate uncertainty on the convection velocity, $\varepsilon_{U_c} = 4\%$, and a small uncertainty on the mean velocity, $\varepsilon_U = 0.5\%$ (middle black line in fig. 1b), TH appears to outperform EU for all velocity uncertainty levels and pLA for uncertainties on the velocity larger than 2%, (fig. 1a). Finally, for a moderate level of uncertainty on both convection and mean velocity $\varepsilon_{U_c} = 4\%$, $\varepsilon_{U_c} = 2\%$, TH shows larger uncertainty with respect to pLA for all velocity uncertainty levels and provides slightly more accurate pressure estimates than EU for velocity measurement uncertainties of 3 and 4%, (upper limit, fig. 1b).

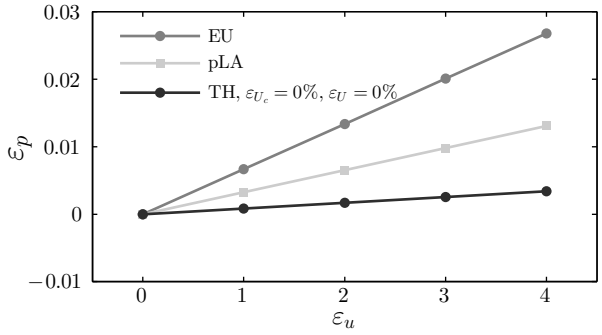

(a)

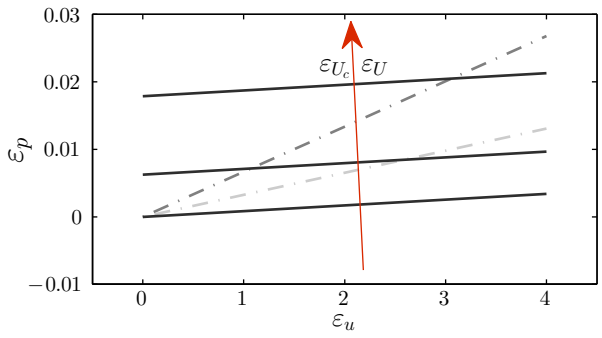

(b)

Fig. 1: Total uncertainty on the pressure estimation following eq. (11)–(13) for all methods (top). Total uncertainty on the pressure estimation for TH with increasing levels of ε_{U_c} and ε_U (bottom)

To conclude, for small uncertainty levels on the convection mean velocity estimation TH can provide a good accuracy for pressure estimation with respect to the other two approaches, especially for high velocity measurement uncertainties (which are likely to occur in high-Reynolds-number measurements due to the large dynamic range in velocity scales).

4 Numerical assessment

The next step is to assess the performance of the methods on synthetic data, therefore we apply them to the John's Hopkins University channel flow database (Li et al, 2008; Perlman et al, 2007; Graham et al, 2013). Since the ultimate goal of this work is to estimate pressure using experimental data, we used this DNS dataset to simulate synthetic 3D PIV velocity snapshots on which we then implemented the different approaches and assessed their accuracy using the provided DNS pressure fields. The main simulation parameters and flow statistics of the original dataset are shown in Table 1. From this dataset, 30 independent time-frames of an initial volume located at the logarithmic layer in the wall normal direction and in the middle of the channel in x and z were chosen. The points were initially interpolated onto an equidistant grid, including an appropriate weighting function to remove the bias due to the initial non-uniform spacing in y. To simulate the averaging effect of PIV (Schrijer and Scarano, 2008), filtering using a Hann window was performed together with the interpolation to avoid aliasing effects and the volumes were subsequently cropped to avoid edge effects. Finally, the noise effect inherent to PIV (Foucaut et al, 2004) was accounted for by adding random noise fields, filtered and cropped as described above, on the velocity data. To assess the methods' dependence on resolution,

Table 1: DNS channel non-dimensional flow simulation parameters

Parameter	**Value**
Friction velocity Reynolds number: $\boldsymbol{Re_\tau}$	999.713
Database timestep: $\boldsymbol{dt^+}$	0.32
Domain Length : $\boldsymbol{L_x} \times \boldsymbol{L_y} \times \boldsymbol{L_z}$	$8\pi h \times 2\pi h \times 3\pi h$
Grid : $\boldsymbol{N_x} \times \boldsymbol{N_y} \times \boldsymbol{N_z}$	$2048 \times 512 \times 1536$

three different filter lengths of $l^+ = 12$, 24, and 48 were used on an equidistant grid with grid spacing of $h^+ = 3$, 6, and 12, simulating an overlap of 75%. Five different noise levels (including the zero noise case) were tested, scaled such that their root-mean-square (rms) value, ε_u, was given as a certain percentage (0, 1, 2, 3, and 4%) of the maximum velocity occurring in the flow (see also de Kat and Ganapathisubramani, 2013).

As mentioned above, TH includes the choice of an appropriate convection velocity (eq. 9). In this work, three different convection velocities were examined. More specifically, both the mean of the streamwise velocity, $U_c = U(y)$, constant in the x–z plane, and the filtered version of it, $U_c = U_f$, (which yielded a locally varying convection velocity field) were tested. A three dimensional convection velocity was also examined, where the values of the three components were the mean values of the respective flow velocity components: $\mathbf{U_c} = U(y), V(y), W(y)$. The mean fields mentioned above, imply time averaging over the selected set of snapshots. Finally, four different time-separations between the frames used for the computation of the acceleration were tested, for EU and pLA. More specifically, for each of the 30 selected time frames, where the pressure was computed, snapshots located one ($n = 1$) up to eight ($n = 8$) time steps before and after were also selected and used to compute the acceleration on the central snapshot.

Because of the large parameter space involved, we first selected the convection velocity and frame time separation that provided the most accurate results for TH and EU and pLA respectively. Using these values, which represented the best performance of each method, we could then compare across the different methods and also assess their dependence on grid resolution and noise levels. Four different performance measures were computed, all with respect to the exact and estimated pressure fields. These were the correlation coefficient between the two fields, their coefficient of determination (R-squared), the normalised variance of their difference, and the mean squared error between their probability density functions. For brevity, since all measures indicated similar behaviour, only the correlation coefficient results will be discussed in the following sections.

4.1 Convection velocity and frame time-separation dependence

For TH, pressure was determined using the three convection velocities outlined above. The resulting fields had a higher average correlation coefficient with the DNS field when the streamwise mean velocity was used as convection velocity (Table 2). Therefore, this was the convection velocity used for the grid and noise resolution dependence study later. This was also in line with results from Geng et al (2015), who showed that for the logarithmic region of the boundary layer, using the mean velocity as the convection velocity is an adequately accurate assumption. For the EU and pLA approaches, pressure fields were estimated using the different time separations to compute acceleration, as outlined above. The results for the average correlation coefficient show that for pLA the most accurate pressure field is the one computed with the largest time frame separation (fig. 2). For EU the noise level present in the data influences the dependence of the method on the time-separation. In the case of $\varepsilon_u/U_{max} = 1\%$ (fig. 2), an increase of time separation up to $dt^+ = 1.28$ results in higher correlation values but the accuracy decreases for larger time-steps. In contrast to that, for the zero noise case, there is a monotonic decrease in correlation as the timestep increases (fig. 3 top line). This is expected since, for EU, an increase of time separation, dt, decreases the precision error, $\frac{\varepsilon_u^2}{2dt^2}$, associated with the uncertainty on the velocity field, but intensifies the truncation error, $\frac{dt^2}{6}\frac{\partial^3 \mathbf{u}}{\partial t}$, stemming from the discretisation scheme (see van Oudheusden, 2013), a behaviour also observed for derivative filters (Foucaut and Stanislas, 2002). Therefore, for good quality data, as is the case of zero noise, it is the truncation error that is more prominent and dictates small time separations to be used. However, for higher noise level (or experimental results), a small increase of dt might pro-

Table 2: Average correlation coefficient with varying convection velocities ($\varepsilon_u/U_{max} = 1\%$, $l^+ = 12$)

	$U_c = U(y)$	$U_c = U_f$	$\mathbf{U_c} = U(y), V(y), W(y)$
r_{p_i}	0.80	0.76	0.76

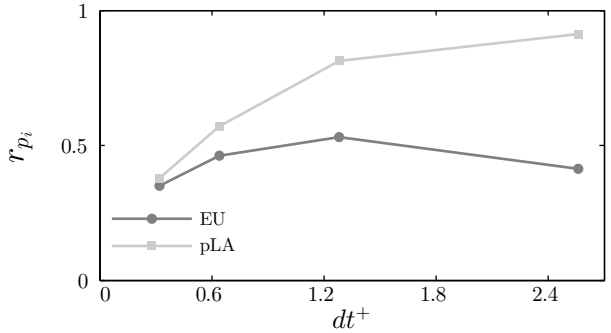

Fig. 2: Average correlation coefficient with varying frame time-separation ($\varepsilon_u/U_{max} = 1\%$, $l^+ = 12$). For pLA the largest timestep yields the best results. The performance of EU improves for moderate time-steps but deteriorates again for the largest dt's used

vide a better balance between the two error sources (fig. 3 middle and bottom line). A larger increase of dt though,

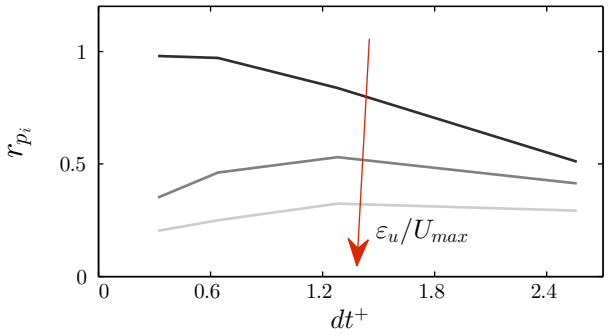

Fig. 3: Average correlation coefficient with varying frame time-separation and noise for EU ($l^+ = 12$). When noise is present in the data a moderate increase in timestep improves the performance, while for zero noise the minimum timestep yields the most accurate results

would lead to an increasing truncation error representing the receding correlation between the velocity fields used for the computation of the acceleration. For an Eulerian approach this would in turn lead to an increasing error on the acceleration. Moreover, the time derivative for the computation of the acceleration implies that an increasing timestep will also lead to aliasing. This explains the drop in correlation for time-steps larger than $dt^+ = 1.28$ for the case of $\varepsilon_u/U_{max} = 1$ and 2% (fig. 3 middle and bottom line). Therefore, for EU, a moderate frame separation is chosen for the rest of the study ($dt^+ = 1.28$). In the case of pLA, even though the largest time separation ($dt^+ = 2.56$) yields the best results, it also leads to a loss of more than 60% of the volume due to fluid parcels leaving the FOV during the reconstruction of the parcels' trajectories. For this reason, we select an intermediate value ($dt^+ = 1.28$) as well, for the rest of the study, where less than 40% of the volume is lost and the method still performs adequately.

4.2 Noise dependence

With the convection velocity and time frame separation chosen, pressure was estimated using all methods for the different noise levels and the average correlation coefficient between the exact and estimated pressure fields with respect to noise was determined (fig. 4). For the zero noise level, pLA provides very accurate results (correlation coefficient close to 1) outperforming TH, which reaches values around 0.8. EU has a slightly lower accuracy than pLA (because, as mentioned above, the timestep selected improves the performance only when noise is present) but still outperforms TH. As noise increases the correlation coefficient follows a decreasing trend for all methods, however TH appears to be the least influenced and outperforms the other two approaches for all noise levels considered. These observations

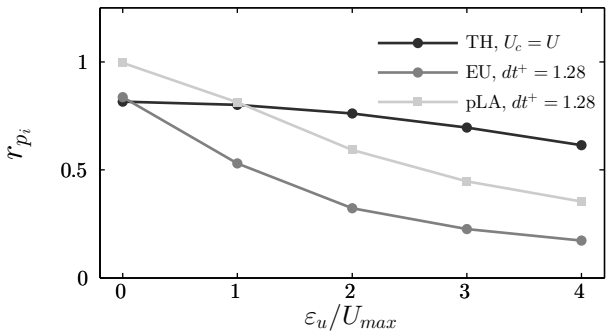

Fig. 4: Average correlation coefficient with varying noise ($l^+ = 12$, $dt^+ = 1.28$ for both EU and pLA). All methods show decrease in correlation with increasing noise with TH being the least sensitive to noise and EU suffering the most

are in line with the uncertainty propagation analysis, where it was shown that for zero noise on the velocity field, pressure estimates with either EU or pLA should not have any uncertainty propagating through (eq. 12 and 13), while pressure estimates using TH can have an uncertainty relating to an incorrect convection velocity chosen, as is the case here. However, as the uncertainty on the velocity increases, EU and pLA suffer significantly more while TH still retains acceptable levels of accuracy even at the largest noise level.

4.3 Resolution dependence

Finally, pressure was estimated for the different grid resolutions outlined above and the average correlation coefficient between the exact and estimated pressure fields was determined (fig.5). Decrease in grid resolution leads to poorer performance for all three methods. Similar to the influence of noise on TH (fig. 3), lower grid resolution results in a decrease of the pressure correlation coefficient from about 0.79 for the best resolution, to about 0.6. EU follows a similar decreasing trend, from a correlation coefficient around 0.53 dropping to 0.3 for the worst resolution. It should also be noted here that it is the noise effect on EU, that is responsible for the much lower values of correlation coefficient with respect to TH. For the pLA approach, there is a much sharper decrease (more than 50%) in accuracy with decreasing resolution which can be of significant importance in the case of experimental data, where high spatial resolution is be hard to attain (especially when time-resolved volumetric velocity fields are required).

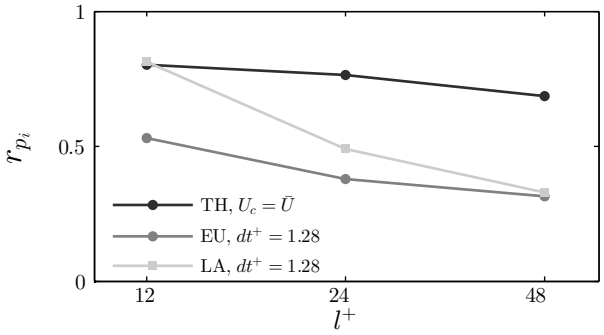

Fig. 5: Average correlation coefficient with varying resolution ($\varepsilon_u/U_{max} = 1\%$, $dt^+ = 1.28$ for both EU and pLA). Decrease in correlation for lower resolution for all methods with TH showing the slowest decrease

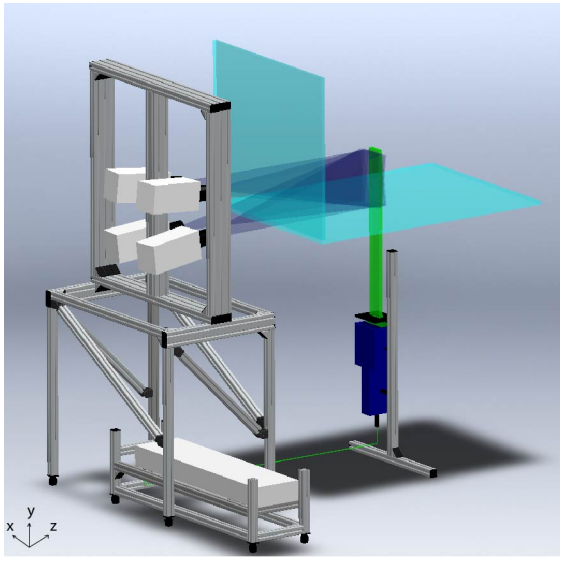

Fig. 6: Schematic (rendering) of the tomographic PIV setup

5 Experimental assessment

For the experimental assessment of the different methods, time-resolved tomographic PIV experiments in a turbulent boundary layer were carried out in the recirculating water tunnel (1.2m $\times$ 0.8m $\times$ 6.75m) located at the University of Southampton Experimental Fluids Laboratory. The measurements were made about 5.5 m downstream of the contraction's end where the flow was tripped (with a 10 cm wide 60-grit sandpaper). For the seeding, 50 μm polyamide particles (Vestosint 2157) were used. A volume, approximately 0.08m $\times$ 0.18m $\times$ 0.02m, in x, y, and z was illuminated with a Litron LDY 304 laser and images were acquired with four Phantom v641 32 GB cameras, with a $2,560 \times 1,600$ pixels sensor, fitted with Sigma f/2.8 EX DG Macro lenses with a focal length of 105 mm, in a cross-like configuration, with a resulting digital resolution of 13 pixels/mm. The bottom two cameras were positioned normal to the volume middle plane, while the top ones were inclined downwards at approximately 10° (fig. 6). The planar angle between both sets of cameras was approximately 15°. A LaVision High Speed Controller was used to synchronise the system. Using DaVis 8.2, we acquired a set of $3,300$ particle images at 1.45 kHz, which we subsequently processed with the same software using an iterative volume correlation with a final interrogation volume of 64 $\times$ 64 $\times$ 64 pixels with an overlap factor of 75%. The nominal flow conditions, based on the 3,300 evaluated vector fields were: $U_\infty \approx 0.66$ m/s, $\delta \approx 0.10$ m, $Re_\tau \approx 2400$, while the resulting FOV was approximately $0.8\delta \times 2\delta \times 0.18\delta$ in the streamwise, wall-normal and spanwise direction respectively (Table 3). The mean velocity profile displayed a logarithmic region ($\kappa = 0.38$, $B = 4.1$ according to Österlund et al, 2000) for $200 < y^+ < 0.15\delta$ (fig. 7). For the computation of the momentum thickness, θ, Spalding's law of the wall (Spalding, 1961) was employed for the region from the wall ($y^+ =$ 0) up to the first independent velocity point (i.e. the first point not influenced by the wall in the volume correlation process).

Table 3: Nominal flow conditions and processing parameters

Parameter	Value
Friction velocity Re number: $\boldsymbol{Re_\tau}$	$2.30 \cdot 10^3$
Momentum thickness Re number: $\boldsymbol{Re_\theta}$	$4.85 \cdot 10^3$
Friction velocity : $\boldsymbol{U_\tau}$	$2.54 \cdot 10^{-2}$ [m $\cdot$ s^{-1}]
Viscosity : ν	$1.16 \cdot 10^{-6}$ [m$^2 \cdot$ s^{-1}]
Domain Length : $\boldsymbol{L_x} \times \boldsymbol{L_y} \times \boldsymbol{L_z}$	$0.8\delta \times 2\delta \times 0.18\delta$ [m]
Interrogation volume size: $\boldsymbol{l_x^+} \times \boldsymbol{l_y^+} \times \boldsymbol{l_z^+}$	$104 \times 104 \times 104$
Timestep: $\boldsymbol{dt^+}$	0.38
Voxel size: $\boldsymbol{l_v^+}$	1.63

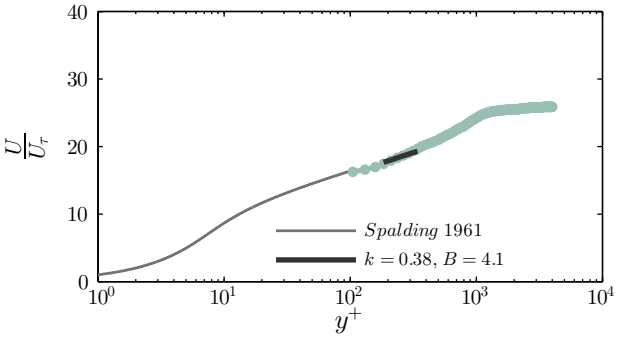

Fig. 7: Inner normalised mean velocity profile

The methods described above were subsequently implemented on the acquired volumetric PIV velocity data using

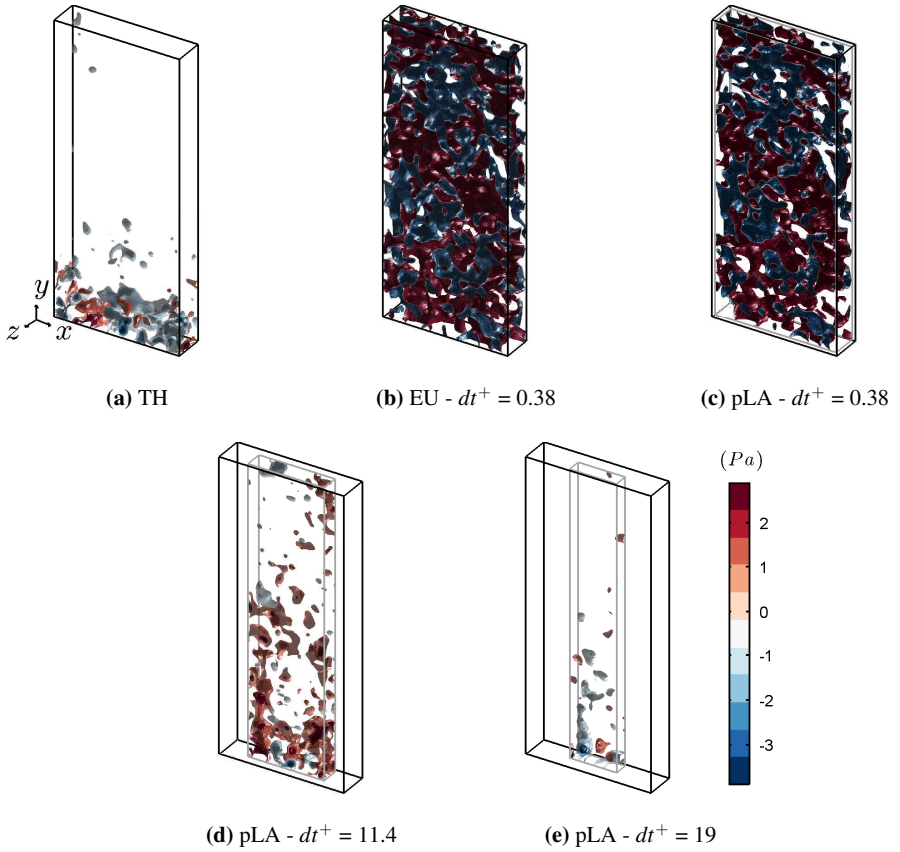

(a) TH **(b)** EU - dt^+ = 0.38 **(c)** pLA - dt^+ = 0.38

(d) pLA - dt^+ = 11.4 **(e)** pLA - dt^+ = 19

Fig. 8: Contour plots of pressure for all methods. Flow is from left to right, axes as appearing on the left, each 200^+ long. TH seems to be the least affected by noise and EU the most while pLA performs much better for very large time-steps but the resulting volume is greatly reduced

the streamwise mean as the convection velocity for TH and initially a single timestep as the frame time-separation for EU and pLA. Since the FOV extended up to the freestream, we could then apply Dirichlet boundary conditions to the top surface of the volumes for the Poisson equation (eq. 2). More specifically, pressure was prescribed ($p = 0$) for a single point at the top surface of the volume, located in the freestream. Additionally, the average pressure of the top surface was also set to zero. Based on the aforementioned nominal flow conditions, the resulting interrogation window size was $l^+ = 104$, much coarser than the different resolutions ($l^+ = 12$, 24, and 48) tested on the DNS dataset, but the time-steps were comparable: $dt^+ = 0.38$ for the experimental dataset and $dt^+ = 0.32$ for DNS.

The results show that for a single timestep ($dt^+ = 0.38$), both pLA and EU are greatly affected from noise (fig. 8b and c), to the point where no individual structures can be identified. The pressure fields using TH (fig. 8a) seem to be less noisy and some individual formations are discernible. This is consistent with the observations of the previous section, where high levels of noise (more than 3%) present in the velocity fields, led to a rapid decrease in accuracy for both EU and pLA approaches (fig. 3), while TH was less influenced. Numerical assessment in the previous section showed that pLA suffered the most with poor spatial resolution (fig. 4). Even for a resolution of $l^+ = 48$, pLA showed a 50% decrease in correlation with the exact pressure field, so we would expect the current resolution of $l^+ = 104$ to be, besides noise, the other main factor responsible for the poor performance (fig. 8c). However, it is also shown that, in terms of frame separation, larger time-steps could potentially improve the performance for pLA (fig. 2), with the limitation being the greatly reduced volumes due to fluid parcels leaving the FOV. To test this observation, we implemented pLA for several different time separations (8d and e). The results show that indeed, for larger time-steps, the evaluated pressure fields are less noisy and some structural details can be detected. Due to the much coarser spatial resolution and high noise levels included, the frame time separation needed in order for pLA to show a marked improvement ($dt^+ = 11.4$) was an order of magnitude larger than the one used for the DNS dataset ($dt^+ = 1.28$). However, also

due to the larger FOV and coarse resolution, the loss in volume due to fluid parcels leaving the FOV was also more limited, which allowed for these large frame separations to be used. Since no reference pressure was available, it was unclear how much these formations, discernible with the Taylor's hypothesis approach and the pseudo-Lagrangian approach, resembled the ones present in the flow. However, we chose to assess the performance of each method using the inner normalised root-mean-square values of pressure $p^+_{rms} = p_{rms}/(\rho U_\tau^2)$—averaged in space and time—and comparing them with DNS results of similar Re numbers. Therefore, pressure distributions from turbulent boundary layers of $Re_\theta = 5000$ ($Re_\tau = 1460$) and $Re_\theta = 6500$ ($Re_\tau = 1990$) (Sillero et al, 2013, 2014; Borrell et al, 2013; Simens et al, 2009) were plotted together with experimental results (figures 9–12). The two DNS datasets were selected so that the former approximately matches the Re_θ of the present experiments and the latter the Re_τ.

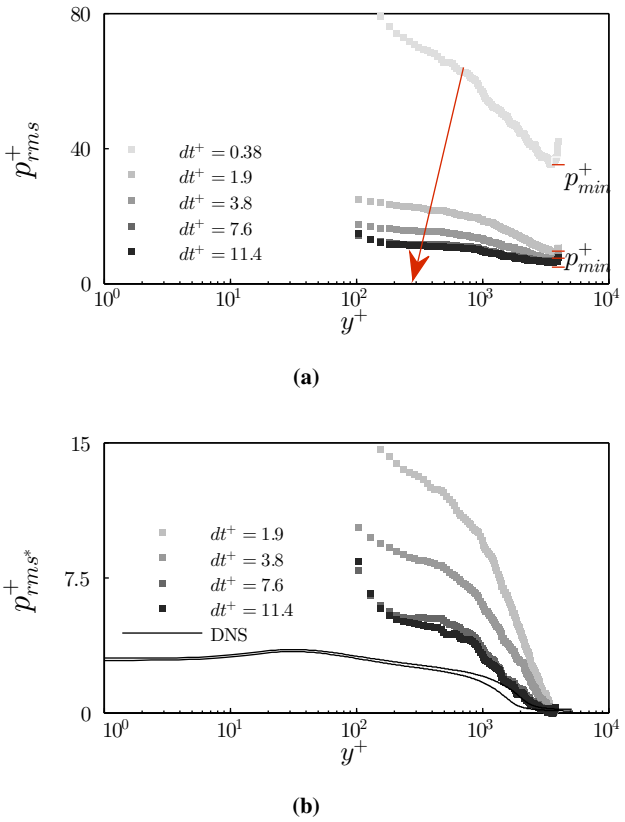

Fig. 9: Root-mean-square pressure, normalised with inner variables, using EU. (a) Results for increasing frame separation ($dt^+ = 0.38$–11.4). (b) Same results translated downwards using a reference pressure and replotted together with DNS (Sillero et al, 2013, 2014; Borrell et al, 2013; Simens et al, 2009) at $Re_\theta = 5000$ ($Re_\tau = 1460$) and $Re_\theta = 6500$ ($Re_\tau = 1990$), solid lines

5.1 Eulerian approach

The numerical study in the previous section showed that EU gave the most accurate results for minimal time separation in case of very good quality data. However, for increasing noise present in the data, as is the case of the experimental results, a moderate increase of timestep improved the performance (fig. 2 and 3). For this reason we tested different time-separations ($dt^+ = 0.38$–11.4) and plotted the resulting pressure fields (fig. 9) together with the DNS data (Sillero et al, 2013, 2014; Borrell et al, 2013; Simens et al, 2009). Results show that for all time separations the pressure values are an order of magnitude higher than the DNS data, in line with the pressure contour plots in fig. 8b. There is however a decreasing trend with increasing frame separation, which is more pronounced between $dt^+ = 0.38$ and $dt^+ = 1.9$. This improvement is—besides the aforementioned decrease in precision error— due to the coarse spatial resolution of the data in conjunction with oversampling in time. For the last two dt's tested ($dt^+ = 7.6$ and 11.4), the near-wall region values deviate significantly from the DNS curve and this could be due to the increasing truncation error (fig. 9a). In the freestream, especially for the smallest frame separation, there was an upward branching of the values, probably due to the boundary conditions imposed. In order to better compare with the DNS data, we removed these end points and subtracted the minimum rms pressure: $p^+_{rms^*} = p^+_{rms} - p^+_{min}$, from all values (see fig. 9a), effectively setting the pressure fluctuations at the freestream to zero. This was a similar–albeit more simplistic–approach to the de-noising of pressure measurements employed by Tsuji et al (2012). The resulting plot (fig. 9b) shows that, even when a constant noise level (corresponding to the p_{min}) is subtracted, the pressure distribution deviates significantly from the DNS data.

5.2 Pseudo-Lagrangian approach

The pressure contours in fig. 8d and 8e and the numerical study results for pLA showed an improvement in performance for increasing time separation, leading however to a decrease in volume. For this reason, similar to EU, we tested several frame separations for pLA and plotted the results together with DNS data (Sillero et al, 2013, 2014; Borrell et al, 2013; Simens et al, 2009). For the first few time-steps used ($dt^+ = 0.38$–7.6), there was a marked improvement with increasing dt^+ as expected, however the overall pressure values were much higher than the DNS data and not shown here. For larger time-steps ($dt^+ = 7.6$–22.8) the values are comparable with the DNS results (fig. 10a), but there is no clear trend with increasing frame separation. As al-

ready mentioned for EU, the maximum allowable timesteps for the method to perform adequately, besides the limitation of volume loss, are also dictated by the combination of a coarse resolution in space with a very high resolution in time. Looking more closely at the area where the experimental points lie (highlighted rectangle in fig. 10a), it is clear that the frame separations that perform best tend to increase with increasing distance from the wall (fig. 10b). It has to be

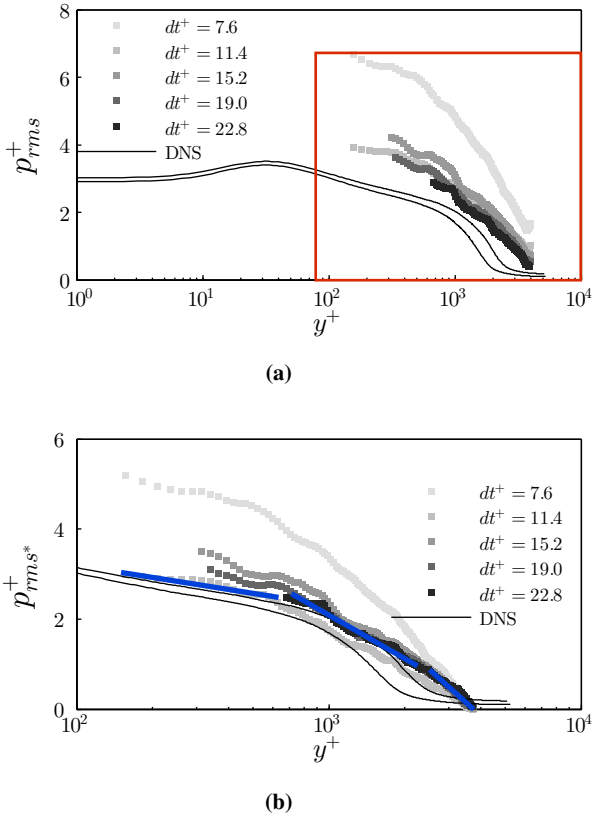

Fig. 10: Root-mean-square pressure, normalised with inner variables, using pLA together with DNS results (Sillero et al, 2013, 2014; Borrell et al, 2013; Simens et al, 2009) at $Re_\theta = 5000$ ($Re_\tau = 1460$) and $Re_\theta = 6500$ ($Re_\tau = 1990$), solid lines. (a) Results for increasing frame separation ($dt^+ = 7.6$–22.8). (b) Zoomed-in region in (a) showing increasing time-scales with increasing y^+

noted that here in favour of consistency, following the same procedure as with the EU results, the end points were removed and the minimum rms pressure was subtracted from the distributions as well. Using $dt^+ = 11.4$ yields the best results for a region up to $y^+ \approx 800$, while for $800 < y^+ < 2500$, the best choice is $dt^+ = 19$ and above that, $dt^+ = 22.8$, even though at that point, the remaining volume is almost reduced to a plane (fig. 10b and 8e). Although the exact limits of these regions are quite uncertain, the general trend agrees with the increase of streamwise velocity away from the wall. Therefore, it is noted that a more suitable implementation of pLA should include a frame separation $dt^+(y^+)$, increasing with y^+.

5.3 Taylor's hypothesis approach

Comparing with the DNS data (Sillero et al, 2013, 2014; Borrell et al, 2013; Simens et al, 2009), shows that TH is the method least influenced by noise and the pressure distribution follows a similar trend as the DNS results (fig. 11). Similar to EU and pLA results, the end points were removed

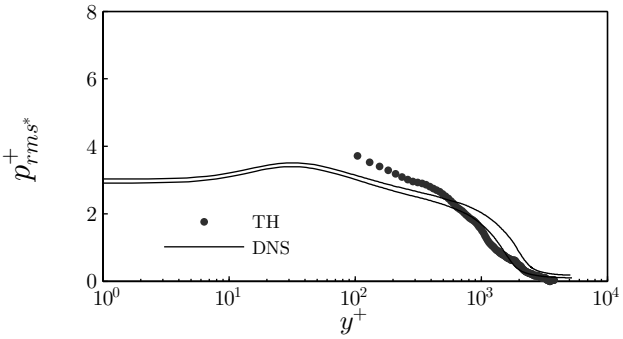

Fig. 11: Root-mean-square pressure, normalised with inner variables, using TH together with DNS results (Sillero et al, 2013, 2014; Borrell et al, 2013; Simens et al, 2009) at $Re_\theta = 5000$ ($Re_\tau = 1460$) and $Re_\theta = 6500$ ($Re_\tau = 1990$), solid lines

and the minimum rms pressure was subtracted from the distribution. With the freestream noise subtraction mentioned above, the rms pressure distribution approximately follows the lower Re DNS dataset (which has a comparable Re_θ with the experimental results), away from the wall. As expected, larger discrepancies can be seen closer to the wall, where the convection velocities likely deviate from the mean (Geng et al, 2015).

5.4 Time and resolution dependence

As already mentioned, the cross-correlation of particle images, which is the core of PIV, acts similar to a low-pass filter in space. In our case the data are also time-resolved and the finite acquisition frequency imposes a similar filter in time. Regarding the spatial filtering effects, unlike the numerical study, where high-resolution data were available and the effects of different filter sizes were evident (fig. 5), the experimental data are already quite coarse in space (l^+ = 104) and even though further decrease of resolution was tested, the effects on the final pressure values were minimal.

The dependence of each method on frame time-separation was already tested above, however to highlight the differences between methods and similar to fig. 2 of the numerical study, the normalised errors (in %) between the estimated and DNS values (Sillero et al, 2013, 2014; Borrell et al, 2013; Simens et al, 2009) were plotted against the different time-steps used (fig. 12). The normalised error, ε^*, is computed for every wall-normal location, y^+, as the average deviation of the estimated pressure values from the two corresponding DNS ones and is then averaged across all y^+ locations. The star denotes the procedure followed in the previous sections where for all approaches, the end points were removed and the minimum rms pressure was subtracted from the distribution. It is also important to note here that, because of the volume losses mentioned above, the error computed for pLA is based on fewer points as the timestep increases. The results show that both EU and pLA approaches improve with larger time-steps, even though for EU the distribution in the near-wall region deviates significantly from the DNS values for very large time-steps (see fig. 9b). When increasing the time-step further ($dt^+ > 10$), the performance of EU starts to deteriorate mirroring the trend of fig. 2 in the numerical study. On the other hand pLA

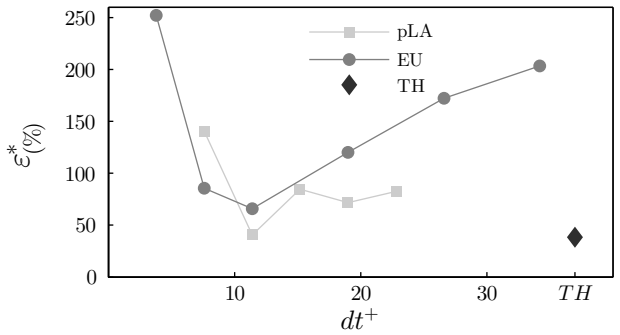

Fig. 12: Average error (in %) of all methods with respect to the DNS results. For pLA a moderate timestep $\sim dt^+ = 10$ yields the best results, even though for larger time-steps the error remains at similar—albeit a bit higher—levels. The performance of EU improves for moderate time-steps but deteriorates again for the largest dt's used. TH is not time dependent and shows quite low error levels

shows lower error levels, some slight oscillations (in line with the behaviour shown in fig. 10b) and the performance does not deteriorate significantly even for the maximum allowable timestep (despite the volume loss). TH does not use time information and is represented by a single point at the right side of the figure, symbolizing the equivalent of an infinite time-step approach. The TH point corresponds to error levels much lower than EU and comparable to pLA when very large time-steps are used. Following the previous observations a $dt^+ = 11.4$ is chosen for both EU and pLA, since it corresponds to the minimum deviation between estimated and DNS distributions for both approaches. With the time-steps chosen, the corresponding pressure distributions of the three approaches can then be compared with each other and the DNS results, as shown in the next section.

5.5 Comparison of all methods

Here, the best results from each method are compared (fig. 13). Both TH and pLA match the low-*Re* DNS dataset, with TH performing better away from the wall, as expected. EU has the poorest performance. Based on the numerical study in the previous sections, the large discrepancies observed for EU can be attributed to the extra velocity term, II, in eq. 12 in the uncertainty analysis. This term does not appear in the uncertainty formulation for pLA, whereas for TH, it involves the magnitude of the velocity fluctuations, $\mathbf{u}'$ and of the difference between the mean and the convection velocity, $\mathbf{U} - \mathbf{U_c}$, which are much smaller. It is obvious that for

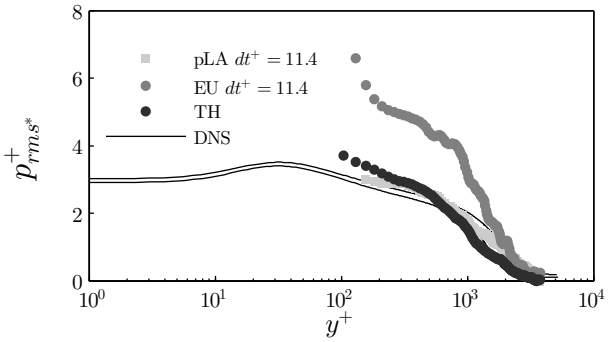

Fig. 13: Comparison of all methods together with DNS results (solid lines) (Sillero et al, 2013, 2014; Borrell et al, 2013; Simens et al, 2009). TH seems to be the least affected by noise while pLA performs much better for large time-steps ($dt^+ = 11.4$) but the resulting volume is greatly reduced

the present experimental conditions, both pLA and TH can provide reasonable results, the former with a considerable loss in volume and noise sensitivity. For pLA it should also be noted that, apart from noise, the coarse resolution might influence significantly the accuracy, based on the results of the numerical study (fig. 4). An experimental dataset with improved resolution could perhaps reveal with more detail whether pLA could improve significantly in performance, or could bring TH within the resolution limits of the DNS study (fig. 4) so that we would be able to predict its accuracy with more certainty. However, we are already reaching

the limits of the state-of-the art equipment and significant improvements in spatial resolution are not possible without losing time resolution or part of the FOV (which would in turn render the Dirichlet condition at the freestream, used in the Poisson formulation, invalid and the pressure estimation less accurate).

6 Conclusions

A concept to determine pressure using Taylor's hypothesis approach for 3C volumetric velocity data was developed and validated numerically, using the channel flow database from John's Hopkins University (Li et al, 2008; Perlman et al, 2007; Graham et al, 2013). Independent synthetic 3C volumetric PIV snapshots were created from the available data and pressure was estimated using a Taylor's hypothesis, an Eulerian and a pseudo-Lagrangian approach. Initially, it was shown that for TH the use of the streamwise mean as the convection velocity yielded the most accurate results. When noise was present in the data, EU performed best using moderate time-steps which provided a balance between truncation and precision errors. The pseudo-Lagrangian approach performed best with increasing time frame separation. For very large separations, even though the accuracy of pLA was improved, there were significant edge effects due to fluid parcel paths outside of the FOV, which resulted in much smaller pressure fields (up to 50%). With the convection velocity and frame time-separation chosen so as to get the best possible results, the dependence of all methods on noise and grid resolution was subsequently tested. It was shown that even though the Eulerian and pseudo-Lagrangian approaches performed better in the case of zero noise and best resolution, their accuracy deteriorated much quicker than the one attained using TH. Especially in the case of high noise levels, both EU and pLA failed completely in determining the pressure, while TH indicated a maximum decrease of correlation of roughly 20%. These results were in agreement with a linear uncertainty propagation procedure for the pressure estimation that was also performed. It was also shown that pLA was the most sensitive of the three methods in terms of grid resolution with a maximum decrease in correlation of more than 50% for a decrease in resolution by a factor of four. Time-resolved volumetric PIV measurements were also performed in a turbulent boundary layer and pressure was estimated on the acquired 3D velocity fields. Results showed that for the minimum time separation, EU and pLA were suffering both from noise and resolution effects, resulting in pressure values an order of magnitude larger than what predicted with DNS at comparable *Re* numbers. For the pressure fields using TH noise effects were limited and some structural formations were discernible, while the rms values of pressure followed closely the distributions from DNS. For larger time-separations, pLA showed a significant improvement, but the resulting volumes were also significantly smaller—in line with the numerical assessment observations. Based on both the numerical and the experimental results, TH seems the most promising approach in these conditions, while pLA can also provide good results for large time separations, increasing with distance from the wall. Experimental data with a higher spatial resolution and of better quality could potentially reinforce these observations, however, large improvements are unlikely due to current limitations in equipment. Better accuracy could also be attained for the Eulerian approach by using more advanced correlation schemes on the 'raw' particle images. Also, as already mentioned above, newly developed fully-Lagrangian techniques can provide very accurate acceleration information which in turn could lead to highly accurate pressure estimations. The important point however, is that for single snapshots of velocity, TH is the only approach of the three than can provide results and even when time information is available, it outperforms EU and has a similar accuracy with pLA without suffering from volume losses.

All data supporting this study are openly available from the University of Southampton repository at `http://dx.doi.org/10.5258/SOTON/385842`

Acknowledgements The research leading to the presented results has received funding from the European Research Council under the European Union's seventh framework program (FP7/2007-2013) / ERC grant agreement no 277472 (WBT project) and grant agreement no 605151 (NIOPLEX project). RdK is supported by a Leverhulme Early Career Fellowship.

References

del Álamo J, Jiménez J (2009) Estimation of turbulent convection velocities and corrections to taylor's approximation. J Fluid Mech 640:5–26

Borrell B, Sillero J, Jiménez J (2013) A code for direct numerical simulation of turbulent boundary layers at high Reynolds numbers in bg/p supercomputers. Computers & Fluids 80:37 – 43, selected contributions of the 23rd International Conference on Parallel Fluid Dynamics ParCFD2011

Charonko J, King C, Smith B, Vlachos P (2010) Assessment of pressure field calculations from particle image velocimetry measurements. Meas Sci Technol 21(10):105401

Davoust S, Jacquin L (2011) Taylor's hypothesis convection velocities from mass conservation equation. Phys Fluids (1994-present) 23(5):051701

Favre A, Gaviglio J, Dumas R (1955) Some measurements of time and space correlation in wind tunnel. Tech.

Rep. NACA-TM-1370, National Advisory Committee for Aeronautics, Washington, DC, United States

Fisher M, Davies P (1964) Correlation measurements in a non-frozen pattern of turbulence. J Fluid Mech 18:97–116

Foucaut J, Carlier J, Stanislas M (2004) PIV optimization for the study of turbulent flow using spectral analysis. Meas Sci Technol 15(6):1046–1058

Foucaut JM, Stanislas M (2002) Some considerations on the accuracy and frequency response of some derivative filters applied to particle image velocimetry vector fields. Meas Sci Technol 13(7):1058–1071

Fujisawa N, Tanahashi S, Srinivas K (2005) Evaluation of pressure field and fluid forces on a circular cylinder with and without rotational oscillation using velocity data from PIV measurement. Meas Sci Technol 16(4):989–996

Geng C, He G, Wang Y, Xu C, Lozano-Durán A, Wallace JM (2015) Taylor's hypothesis in turbulent channel flow considered using a transport equation analysis. Phys Fluids (1994-present) 27(2):025111

Ghaemi S, Ragni D, Scarano F (2012) PIV-based pressure fluctuations in the turbulent boundary layer. Exp Fluids 53(6):1823–1840

Graham J, Lee M, Malaya N, Moser R, Eyink G, Meneveau C, Kanov K, Burns R, Szalay A (2013) Turbulent channel data set available at: http://turbulence.pha.jhu.edu/docs/readme-channel.pdf

Gurka R, Liberzon A, Hefetz D, Rubinstein D, Shavit U (1999) Computation of pressure distribution using PIV velocity data. In: Proc. of the 3rd International Workshop on Particle Image Velocimetry, Santa Barbara, CA

Jakobsen M, Dewhirst T, Greated C (1997) Particle image velocimetry for predictions of acceleration fields and force within fluid flows. Meas Sci Technol 8(12):1502–1516

JCGM 100:2008 (2008) Evaluation of measurement data –Guide to the expression of uncertainty in measurement JCGM 100:2008 (GUM 1995 with minor corrections), Paris

de Kat R, Ganapathisubramani B (2013) Pressure from particle image velocimetry for convective flows: a taylor's hypothesis approach. Meas Sci Technol 24:024002

de Kat R, van Oudheusden B (2012) Instantaneous planar pressure determination from PIV in turbulent flow. Exp Fluids 52(5):1089–1106

de Kat R, van Oudheusden B, Scarano F (2008) Instantaneous planar pressure field determination around a square-section cylinder based on time-resolved stereo-PIV. In: Proc. of the 14th Int Symp on Applications of Laser Techniques to Fluid Mechanics, Lisbon, Portugal

Kim J, Hussain F (1993) Propagation velocity of perturbations in turbulent channel flow. Phys Fluids A: Fluid Dynamics (1989-1993) 5(3):695–706

Krogstad PÅ, Kaspersen J, Rimestad S (1998) Convection velocities in a turbulent boundary layer. Phys Fluids 10(4):949–957

Li Y, Perlman E, Wan M, Yang Y, Meneveau C, Burns R, Chen S, Szalay A, Eyink G (2008) A public turbulence database cluster and applications to study lagrangian evolution of velocity increments in turbulence. J Turbulence 9(31):1–29

Lin C (1953) On taylor's hypothesis and the acceleration terms in the navier-stokes equations. Quart Appl Math 10(4):295–306

Liu X, Katz J (2006) Instantaneous pressure and material acceleration measurements using a four-exposure PIV system. Exp Fluids 41(2):227–240

Österlund J, Johansson A, Nagib H, Hites M (2000) A note on the overlap region in turbulent boundary layers. Phys Fluids 12(1):1–4

van Oudheusden B (2013) PIV based pressure measurement. Meas Sci Technol 24(3):032001

Perlman E, Burns R, Li Y, Meneveau C (2007) Data exploration of turbulence simulations using a database cluster. In: Proceedings of the 2007 ACM/IEEE in Supercomputing, pp 1–11

Schanz D, Schröder A, Gesemann S, Michaelis D, Wieneke B (2013) 'Shake the box': A highly efficient and accurate Tomographic Particle Tracking Velocimetry (Tomo-PTV) method using prediction of particle positions. In: Proc. of the 10th Int Symp on Particle Image Velocimetry, Delft, The Netherlands

Schanz D, Schröder A, Gesemann S (2014) 'Shake the box' - a 4D-PTV algorithm: Accurate and ghostless reconstruction of Lagrangian tracks in densely seeded flows. In: Proc. of the 16th Int Symp on Applications of Laser Techniques to Fluid Mechanics, Lisbon, Portugal

Schrijer F, Scarano F (2008) Effect of predictor–corrector filtering on the stability and spatial resolution of iterative piv interrogation. Exp Fluids 45(5):927–941

Sillero J, Jiménez J, Moser R (2013) One-point statistics for turbulent wall-bounded flows at Reynolds numbers up to $\delta^+ \approx 2000$. Phys Fluids 25(10):105102

Sillero J, Jiménez J, Moser R (2014) Two-point statistics for turbulent boundary layers and channels at Reynolds numbers up to $\delta^+ \approx 2000$. Phys Fluids 26(10):105109

Simens MP, Jiménez J, Hoyas S, Mizuno Y (2009) A high-resolution code for turbulent boundary layers. J Comput Phys 228(11):4218–4231

Spalding D (1961) A single formula for the law of the wall. J Appl Mech 28(3):455–458

Taylor G (1938) The spectrum of turbulence. Proc R Soc Lond A 164(919):476–490

Tsuji Y, Imayama S, Schlatter P, Alfredsson PH, Johansson A, Marusic I, Hutchins N, Monty J (2012) Pressure fluctuation in high-Reynolds-number turbulent boundary

layer: results from experiments and DNS. J Turbulence 13(50):1–19

Violato D, Moore P, Scarano F (2010) Lagrangian and eulerian pressure field evaluation of rod-airfoil flow from time-resolved tomographic PIV. Exp Fluids 50(4):1057–1070

Zaman K, Hussain A (1981) Taylor hypothesis and large-scale coherent structures. J Fluid Mech 112:379–396